

# Stretch-inactivated ion transport through subnanoporous two-dimensional membranes

Yechan Noh

*Department of Physics, University of Colorado Boulder, Boulder, CO 80309, USA\**  
*Applied Chemicals and Materials Division, National Institute of Standards and Technology, Boulder, CO 80305, USA\* and*  
*Department of Materials Science and Engineering,*  
*University of California Berkeley, Berkeley, CA 94720, USA*

Alex Smolyanitsky<sup>†</sup>

*Applied Chemicals and Materials Division, National Institute of Standards and Technology, Boulder, CO 80305, USA*

(Dated: October 16, 2024)

In biology, mechanosensitive ion channels facilitate the conversion of mechanical stimuli, such as sound and touch, into electrical signals. Similar functionality in artificial systems was recently predicted in the form of stretch-*activated* transport through porous 2D membranes. Here we describe an opposite behavior, in which ion transport is *inactivated* upon stretching a sub-nanoporous 2D membrane. We explore electrophoretic ion transport through several subnanoporous membranes using molecular dynamics simulations. We demonstrate that aqueous  $K^+$  transport *decreases* by a factor of 3-8 under stretching of order 3 %. In contrast,  $Na^+$  ions exhibit transport activation by stretching, suggesting ion-dependent activation and inactivation in a single membrane. Our analysis shows that inactivation of  $K^+$  transport is caused by a strain-induced repulsive-to-attractive transition in the  $K^+$ -pore interactions due to alignment of the local energy minima.

Mechanosensitive protein ion channels convert mechanical inputs into electrical and biochemical signals [1–3], facilitating critical functions such as tactile sensation, auditory perception, osmoregulation, and neural signal processing. Achieving similar functionality in synthetic membranes is an important milestone for engineering advanced nanofluidic devices. Recent efforts have yielded potentially promising demonstrations of strain- and pressure-induced ion transport *activation* in synthetic systems. These include strain-sensitive activation of ion transport in two-dimensional (2D) membranes [4–8], pressure-gating in conical nanopores [9], and transport modulation through pressure-voltage coupling [10, 11]. The opposite behavior, wherein transport is *deactivated* by tensile stretching of the channel-hosting membrane, so far has only been observed in biological protein ion channels [12–15]. Importantly, protein ion channels often undergo intricate structural transformations under strains applied to the channel-hosting lipid membrane [1, 2, 16]. For their synthetic solid counterparts, however, membrane stretching is expected to transduce directly into pore dilation and thus stretch-inactivated transport has been neither explored, nor does it appear to be intuitively expected.

To improve our basic understanding of transport through sub-nanoscale pores, here we demonstrate distinct stretch-inactivated ion transport in sub-nanoporous solid 2D membranes and describe the underlying mechanisms. We investigated ion transport through sub-nanoporous solid membranes under tensile strain using

molecular dynamics (MD) simulations. The porous membranes we considered include a locally suspended hBN monolayer hosting  $B_3N$  multivacancies [17, 18] and a  $C_2N$  monolayer featuring naturally occurring hexagonal pores [19–21], shown in Figs. 1 (a-c) alongside the corresponding pore structures. The atoms at the membrane perimeters were tethered to their initial positions using harmonic restraints to prevent membrane drifting. The membranes were solvated in an aqueous electrolyte inside a roughly cubic  $XYZ$ -periodic box with a 6-nm-long side for hBN and  $4.4\text{ nm} \times 4.2\text{ nm} \times 6\text{ nm}$  for  $C_2N$ . The explicit water molecules were simulated according to the TIP4P model [22]. The OPLS-AA forcefield [23] was used to describe all bonded and non-bonded interactions involving hBN [24] and  $C_2N$  [21]. The partial atomic charges of the pore edge nitrogens (each with two nearest-neighbor boron atoms instead of three in bulk hBN) were set to  $2/3$  of the bulk values quantum-chemically derived in earlier work [24], resulting in charge neutrality of the pore regions. The non-bonded parameterization for  $C_2N$  was set according to the OPLS-AA forcefield, with the atomic charges derived using the CHELPG scheme [25], applied at the HF/6-31+G(d) theory level [26, 27] for the optimized membrane geometry and yielding  $q_N = -0.44e$ ,  $q_C = +0.22e$ . Prior to ion transport simulations, all systems underwent static energy minimization and 10 ns of NPT relaxation at  $T = 300\text{ K}$  and  $P = 1\text{ bar}$ , during which the box height along  $Z$  was adjusted, while  $XY$ -dimensions were kept constant. All production simulations were carried out in the NVT ensemble. To facilitate ion transport, a constant electric field was applied along  $Z$  and the data were collected over 200–500 ns of simulated time. All MD simulations were performed using the GPU-accelerated GROMACS package v.2023.2 [28, 29].

Consider Fig. 1 (e), where ion transport through  $B_3N$

---

\*Current affiliation: University of Colorado Boulder and National Institute of Standards and Technology

<sup>†</sup>Corresponding author: alex.smolyanitsky@nist.gov

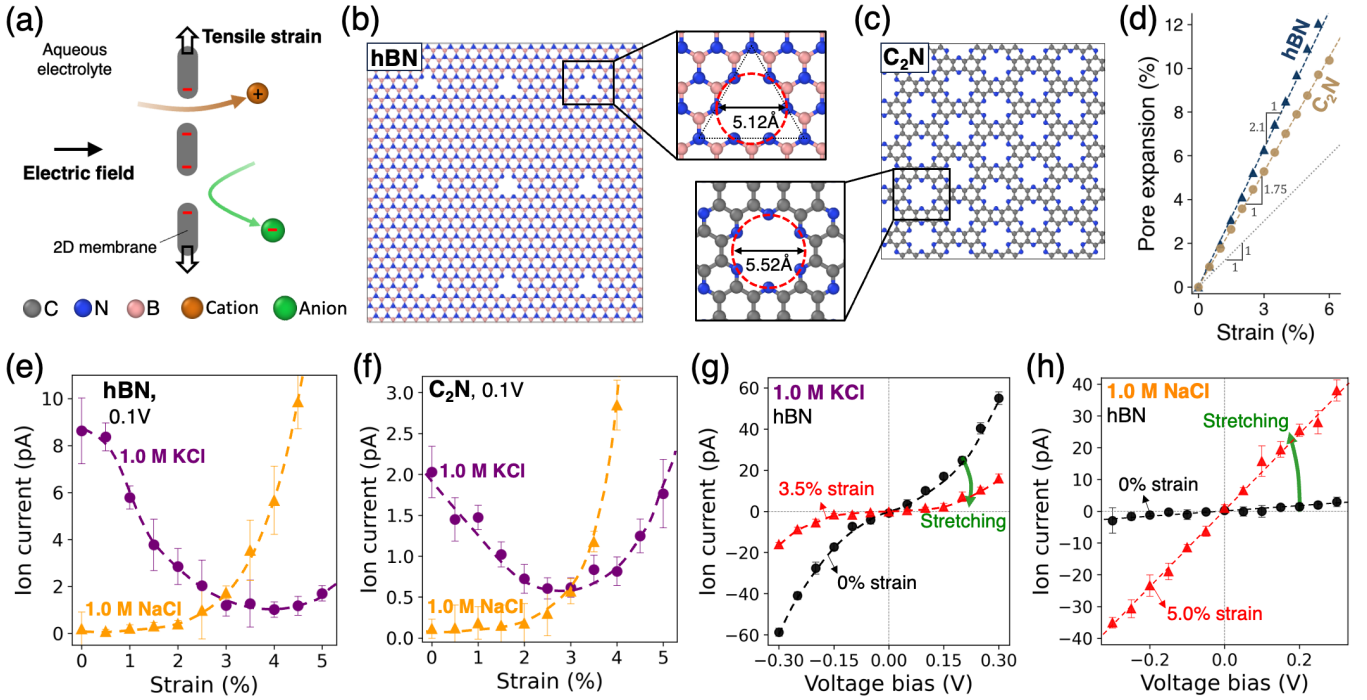


FIG. 1: Mechanosensitive ion transport through triangular  $B_3N$  defects in hBN and porous  $C_2N$  monolayers. A sketch of anion/cation transport selectivity for pores featuring dipolar electrostatics at the edge (a). The color-shaded spheres represent the atomic/ionic species in this work. Membrane and pore structures for  $B_3N$ -defective hBN (b) and  $C_2N$  monolayers (c). Pore dilation as a function of membrane strain (d). Stretch-inactivated ion conduction through hBN membrane (e) and  $C_2N$  membrane (f) in single-salt 1.0 M KCl and NaCl. The error bars for each current data point are standard deviations from 1-ns-long subsets of flux data used to calculate the ion currents. Current-voltage curves for the activated and inactivated state of hBN membrane in (f) 1.0 M KCl and (g) 1.0 M NaCl.

vacancies in hBN is described for 1.0 M single-salt concentrations of KCl and NaCl under a transmembrane voltage equivalent of 0.1 V. Due to small effective pore diameter and the resulting strong dipolar electrostatics featuring negative charges at the pore edge, anions are rejected completely, while cations ( $K^+$  and  $Na^+$ ) permeate (see sketch in Fig. 1 (a)). We define mechanosensitivity as  $\mu = \frac{dI}{d\varepsilon}$ , where  $I$  and  $\varepsilon$  are the ion current and the membrane strain. As shown, the response of the ion current to the membrane strain for KCl and NaCl solution exhibits a striking contrast: upon membrane stretching, we observe  $\mu < 0$  for KCl and  $\mu > 0$  for NaCl. More specifically,  $K^+$  is shown to *decrease* by a factor of 8.4 at  $\varepsilon = 3.5\%$ , presenting a case of transport inactivation by stretching. With strains increasing further, a more intuitively expected  $\mu > 0$  behavior emerges at  $\varepsilon > 3.5\%$ . For  $Na^+$  we observe  $\mu > 0$  throughout the entire range of considered  $\varepsilon$ , causing a 89-fold increase at  $\varepsilon = 6\%$ . Regardless of any strains applied,  $Cl^-$  ions remained rejected. Note that an opposite set of trends was reported for 18-crown-6 pores in aqueous KCl, where  $K^+$  current *increased* to a local maximum before decreasing at strains significantly larger than 3% [6]. Contrasting permeation behaviors are also exhibited by the  $C_2N$  membrane, with  $K^+$  transport reduced by a factor of 3.4 near  $\varepsilon = 3.0\%$  and  $Na^+$  transport increased by a factor of 61 at  $\varepsilon = 6.0\%$ . In addition to Figs. 1 (e,f), please refer to the Sup-

plementary Material [30] (and references [31–35] therein). In particular, see supplementary Fig. S1 for ion currents at the full range of applied strains.

In order to understand the basic mechanisms underlying the phenomena described above, we start by determining whether the pores in fact dilate during membrane stretching. Without strain, the pore diameters defined in Fig. 1 (b) and (c) are 5.12 Å and 5.52 Å for the  $B_3N$  vacancy and the  $C_2N$  pore, respectively. As shown in Fig. 1 (d), pore dilation is  $\alpha\varepsilon$ , where  $\alpha$  is a material-specific pore dilation factor of  $\approx 2.1$  and  $\approx 1.75$  for the  $B_3N$  vacancy and the  $C_2N$  pore, respectively. The values  $\alpha > 1$  suggest a degree of softness in the porous regions, relative to the membrane as a whole, as expected. Pore widening in direct proportion to membrane strain indicates that inactivation of  $K^+$  transport for both hBN and  $C_2N$  indeed takes place during pore enlargement by order  $2\varepsilon$ . The observed levels of transport modification in response to such modest geometry changes can not be explained within the diffusive transport paradigm and thus it has been broadly proposed that for sub-nm pores ion transport is governed by local barriers [4–6, 8], thus making the permeation rate an Arrhenius exponent  $e^{-\frac{\Delta E}{k_B T}}$  of the strain-dependent transport barrier  $\Delta E$  ( $k_B$  is the Boltzmann constant and  $T$  is the system temperature). Consequently, strain-induced modifications of  $\Delta E$  even of order few  $k_B T$  can modulate the permeation rate significantly.

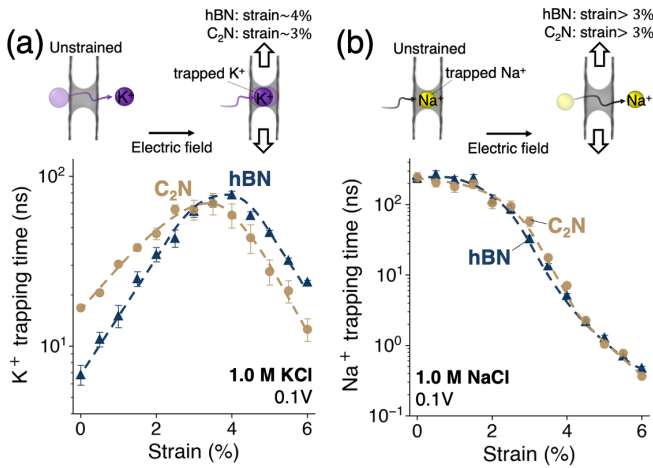


FIG. 2: Contrasting behavior of  $K^+$  and  $Na^+$  trapping under membrane stretching. Ion trapping times *vs* membrane strain for  $K^+$  (a) and  $Na^+$  (b), along with the qualitative illustrations at the top of each panel. The ion trapping time is determined based on the average residence time within the pore region, which is defined as being within  $3.5 \text{ \AA}$  on either side of  $Z = 0$  from the pore center in  $Z$ -coordinate. The error bars are standard deviations for the time-averaged trapping times.

As shown further, these barriers can in fact increase upon pore dilation, leading to distinct transport inactivation. To further demonstrate barrier-driven transport, shown in Fig. 2 (a) are the effective times spent by  $K^+$  trapped inside the hBN- and  $C_2N$ -based pores as a function of membrane strain (given the pore size, only one ion at a time “fits” inside). At  $\varepsilon = 0$ ,  $K^+$  ions spend  $\approx 7 \text{ ns}$  and  $\approx 16 \text{ ns}$  in hBN and  $C_2N$  pores, respectively, increasing significantly at the peaks of the corresponding curves. In contrast, as shown in Fig. 2 (b) for both membrane materials,  $Na^+$  ions are stably trapped at  $\varepsilon = 0$  and feature decreasing trends as a function of strain, similarly to crown pores in graphene [4, 6]. The permeation timings will be revisited further in the text.

The transport barrier energetics in the case of porous hBN is considered in Fig. 3 (a-c), where we plot the free energy profiles of  $K^+$  and  $Na^+$  ions along the transport coordinate in the  $Z$ -direction. These profiles are in the form of potential mean force (PMF) curves, as calculated using the weighted histogram analysis method (WHAM) [36] for various strain values. Fig. 3 (a) shows the PMF for  $K^+$  within the strain range corresponding to  $\mu < 0$ . At  $\varepsilon = 0$ , the PMF exhibits two local minima located on either side of the pore, separated by a minor local maximum at  $Z = 0$ , arising from the van der Waals ion-pore interactions. Upon membrane stretching, the repulsive component at  $Z = 0$  becomes progressively smaller, while the minima themselves deepen to explain the increasing ion-pore affinity as  $\varepsilon$  increases. Notably, at 4 % strain, the two minima coalesce into essentially a single well. In Fig. 3 (b) we show the PMF for  $K^+$  at higher yet strains. In this regime, a more familiar  $\mu > 0$  trend in line with previous reports [4–6] is re-

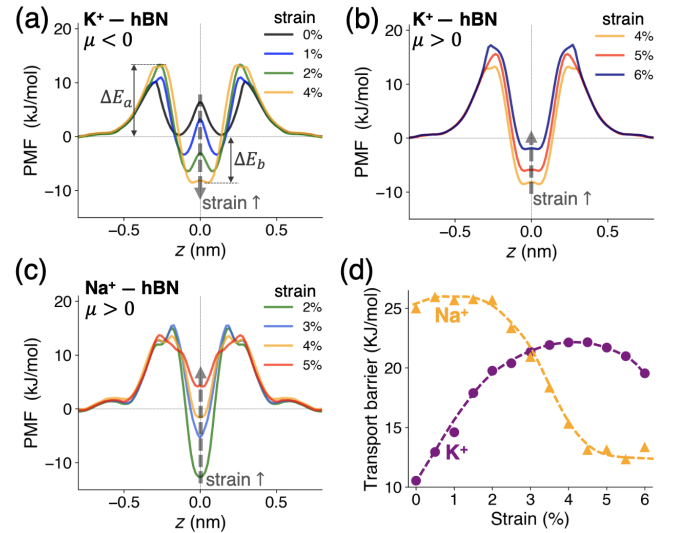


FIG. 3: Free energy analysis for the hBN membrane. PMF profiles of  $K^+$  ion along the transport coordinate for various strains in the strain ranges of  $\mu < 0$  (a) and  $\mu > 0$  (b). (c) PMF profile of  $Na^+$  ion at various strain magnitudes. (d) Transport barrier (the sum of  $\Delta E_a$  and  $\Delta E_b$  defined in (a)) of  $K^+$  and  $Na^+$  *vs* membrane strain.

covered, as the central attractive well starts to become more shallow. For  $Na^+$  ions in Fig. 3 (c), the behavior is essentially the same as that in Fig. 3 (b) for  $K^+$ . As expected, the energetics and the permeation timings behave quite similarly for  $C_2N$ , as shown in supplementary section S2 [30]. Finally, in Fig. 3 (d) we show the magnitude of the transport-limiting barrier  $\Delta E = \Delta E_a + \Delta E_b$  (defined in Fig. 3 (a)) for  $K^+$  and  $Na^+$  permeating porous hBN at various strains. Contrasting trends in direct correlation with the transport *vs* strain curves in Figs. 1 (e,f) are observed. The analysis above provides insight into the barrier-transport relationship for the observed transport trends and leads us to the key question of the mechanisms behind the strain-induced enhancement and weakening of the ion-pore affinity for  $K^+$  and  $Na^+$ , respectively.

The origin of strain-induced barrier enhancement observed here is of basic interest regardless of the two materials considered in this work, as they merely represent examples of pores of suitable size and composition. Although the dehydration component of the barrier  $\propto \frac{1}{r}$  ( $r$  is the effective pore radius) is expected to contribute to enhancement near  $Z = 0$  [4], it can be shown that this contribution can not compete against the weakening dipolar ion-pore electrostatics  $\propto -\frac{1}{r^2}$  (see Supplementary section S3 [30]). To fully describe the primary mechanism underlying the observed strain-induced transport inactivation, we therefore consider the total energy of ion-pore interactions, including first-order Coulomb and van der Waals contributions. Consider the ion-pore potential contributions shown in Fig. 4 (a) for hBN and in Fig. 4 (b) for  $C_2N$ , plotted as a function of  $X$  coordinate for an ion at  $Z = 0$ . The green and red curves

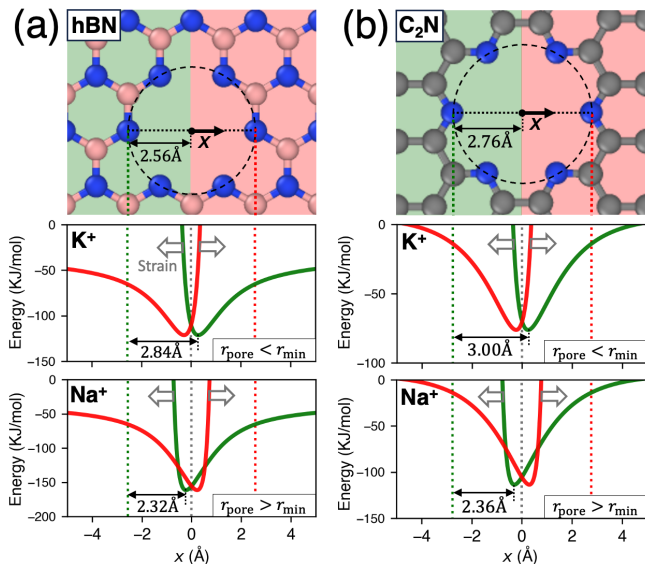


FIG. 4: Overlapping potential minima of the ion-pore interactions for hBN (a) and  $C_2N$  (b) membranes for  $K^+$  and  $Na^+$  ions. The green and red curves are contributed by the respectively colored shaded regions shown in the top sections of each panel. The arrows next to each curve shows that upon pore dilation the green and red curve shifts left and right, respectively.

correspond to the energies contributed by the atoms in the green- and red-colored membrane halves in the top panels, respectively. The sum of Coulomb and van der Waals interactions (given by the Lennard-Jones potential in this case) yields local energy minima at specific distances from the corresponding nearest edge atoms. Here, the distances between the potential energy minima and the nearest edge nitrogens are denoted  $r_{min}$ , while the pore radius  $r_{pore} = 2.56 \text{ \AA}$  for the unstrained hBN membrane is as defined in Fig. 1 (b). For  $K^+$ , at  $\varepsilon = 0$ ,  $r_{min} = 2.84 \text{ \AA}$  and thus  $r_{pore} < r_{min}$ , resulting in a misalignment between the energy minima. For unstrained  $C_2N$  in Fig. 4 (b),  $r_{pore} = 2.76 \text{ \AA}$  and  $r_{min} = 3.00 \text{ \AA}$ , also satisfying  $r_{pore} < r_{min}$ . As the pores dilate due to membrane stretching, the potential energy minima become aligned, resulting in *enhanced* ion-pore binding. Specifically, for  $K^+$  inside an hBN pore, at  $\varepsilon = 4 \%$ , the pore becomes dilated by  $\approx 8.4\%$ , corresponding to  $r_{pore} \approx 2.78 \text{ \AA}$ , which closely matches  $r_{min} = 2.84 \text{ \AA}$  and yields the strongest possible ion-pore binding in this case. For  $C_2N$ , this matching occurs near  $\varepsilon = 4.5 \%$ . Although in reasonable agreement with the minimum of the current located at  $\varepsilon = 3.0 \%$ , discrepancies may arise between the strains yielding the vacuum energy minima and the minima of the ion current, as discussed later. For both materials, further membrane stretching splits the locations of the minima, leading to a shallower total energy minimum and weakened ion-pore interactions observed at higher yet strains.

In contrast, as shown for  $Na^+$  in the bottom panels of Fig. 4 (a) and (b), the values of  $r_{min}$  are  $2.32 \text{ \AA}$  for

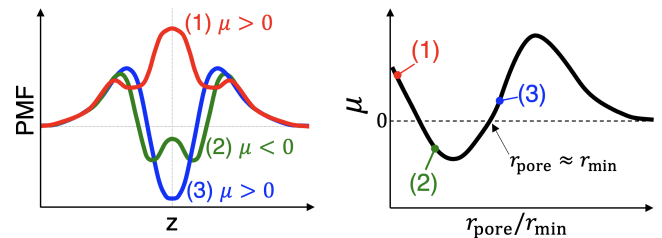


FIG. 5: A qualitative sketch of the mechanosensitive regimes, with strongly attractive and repulsive case corresponding to  $\mu > 0$  and a transition case corresponding to  $\mu < 0$ .

hBN pores and  $2.36 \text{ \AA}$  for  $C_2N$ , corresponding in both cases to  $r_{pore} > r_{min}$ . Here, pore dilation can only further split the minima, weakening the ion-pore interactions upon stretching. In fact, at  $r_{pore} > r_{min}$  only pore compression may lead to the above-described alignment of the minima, unlikely for 2D membranes due to buckling. As expected, this in-plane alignment of the local energy minima readily leads to enhancement of the ion-pore interaction when probed along the  $Z$ -direction (see supplementary Figs. S5-7 [30]), consistent with the data in Fig. 3 (a). Thus, the observed negative mechanosensitivity of  $K^+$  results from a strain-induced transition from weakly repulsive/neutral to weakly attractive ion-pore interactions. It is important to note that the observed transition is not merely a result of MD forcefield parameters used in this work. As described in the supplementary Fig. S7 and the accompanying discussion for  $C_2N$ , quantum-chemical calculations support our MD-based observations [30]. One also notes that the condition  $r_{pore} < r_{min}$  used above for illustration is too broad to accurately describe  $\mu < 0$ , because it includes a case with a strong repulsive peak at  $Z = 0$ , likely resulting in  $\mu > 0$  [5]. The transition region of interest must then be refined to  $(1 - \kappa_t) < \frac{r_{pore}}{r_{min}} < 1$ , where  $\kappa_t$  is an ion-specific constant for each pore, setting the width of the transition region. For the  $\mu < 0$  regions above, it sets the membrane strain required to reach  $r_{pore} = r_{min}$  at  $\varepsilon_{max} = \kappa_t/\alpha$  (of order 3%), where  $\alpha$  is the pore dilation factor of order 2, as estimated above. The strong repulsive and attractive regimes (both featuring  $\mu > 0$ ) are then characterized by  $\frac{r_{pore}}{r_{min}} < (1 - \kappa_t)$  and  $\frac{r_{pore}}{r_{min}} > 1$ , respectively. A sketch of this oscillatory behavior is shown in Fig. 5.

Although the  $(1 - \kappa_t) < \frac{r_{pore}}{r_{min}} < 1$  criterion above establishes negative mechanosensitivity at a basic level, dissociation-limited transport is required to *observe* mechanosensitivity in ion-trapping pores. As discussed in the supplementary section S4 [30], dissociation-limited transport occurs when  $\Delta E_b$  (defined in Fig. 3 (a)) is below  $k_B T \ln(\frac{c_0}{\lambda})$ , where  $\lambda$  is an ion-specific constant for a given energy well and  $c_0$  is the bulk ion concentration. A fit of the pore occupancy data (see supplementary section S4 [30]) suggests  $\lambda_{K^+} = 4.78 \text{ M}$  and  $\lambda_{Na^+} = 0.37 \text{ M}$ , at  $c_0 = 1.0 \text{ M}$  yielding  $\Delta E_b < k_B T$  for  $K^+$  and  $\Delta E_b < -1.56 k_B T$  for  $Na^+$ . The concentration dependence for the condition itself is reasonably weak, at  $0.1 \text{ M}$  yielding  $\Delta E_b < -1.31 k_B T$  and  $\Delta E_b <$

$-3.87k_B T$  for  $K^+$  and  $Na^+$ , respectively. Nevertheless, these bounds on  $\Delta E_b$  are important, because they suggest that the observability of strain-induced transport activation/inactivation generally increases with increasing ion concentration. Conversely, at very low ion concentrations (unlikely to be achievable in *e.g.*, state-of-the-art MD simulations), mechanosensitivity is expected to cease per discussion above – even if  $\Delta E_b$  itself remains strain-sensitive. It is also important to note that the requirement here is not to merely ensure a local well near  $Z = 0$ , because the latter is achievable with  $\Delta E_b > 0$  (see Fig. 3 (a) and supplementary Fig. S8 (a) [30]), leading to weakly strain-dependent  $\Delta E_a$  as the rate-setting barrier. The proposed requirement instead ensures that for ions trapped in the pores the probability of spontaneous desorption is considerably lower than that for ions in the solvent approaching empty pores to cross  $\Delta E_a$ . Therefore, the bound on  $\Delta E_b$  allows for mechanosensitivity to be observed, while the conditions imposed on the ion-pore interactions determine whether transport increases or decreases as a function of strain, as sketched in Fig. 5.

In summary, we utilized MD simulations to demonstrate stretch-sensitive inactivation, as well as activation of aqueous ion transport through subnanoscale pores exemplified by triangular  $B_3N$  vacancy defects in a locally suspended hBN monolayer and a subnanoporous  $C_2N$  membrane. More specifically, we observed contrasting

responses of ion current to membrane strain for  $K^+$  and  $Na^+$  ions. For aqueous  $K^+$ , the ion currents *decreased* by a factor of  $\approx 8$  for the hBN membrane stretched by 4% and by a factor of  $\approx 3.4$  for the  $C_2N$  membrane stretched by  $\approx 3\%$ . This inactivation was attributed to ion-pore interaction *enhancement* upon pore dilation. Conversely, aqueous  $Na^+$  transport increased by well over an order magnitude for both porous structures upon reaching strains of order 6%, due to ion-pore interactions *weakened* by pore dilation. The underlying mechanisms of these contrasting transport behaviors involve alignment of the local energy minima in the repulsive-attractive transition regime, suggesting that atomic-level engineering of sub-nm pores in 2D materials may lead to artificial ion channels featuring positive and negative mechanosensitivity for a rich variety of permeants.

This work was supported in part by the research grant awarded by the National Science Foundation (NSF) under Award No. 2110924, and by computational resources from NSF-supported ACCESS program under Award No. NNT230006. A large portion of the computations for this research was conducted using the high-performance computing facilities at the National Institute of Standards and Technology. The authors are grateful to Andrei Kazakov for illuminating discussions.

- 
- [1] B. Martinac, *Journal of cell science* **117**, 2449 (2004).  
 [2] E. S. Haswell, R. Phillips, and D. C. Rees, *Structure* **19**, 1356 (2011).  
 [3] R. Peyronnet, D. Tran, T. Girault, and J.-M. Frachisse, *Frontiers in plant science* **5**, 558 (2014).  
 [4] A. Fang, K. Kroenlein, D. Riccardi, and A. Smolyanitsky, *Nature Materials* **18**, 76 (2019).  
 [5] A. Fang, K. Kroenlein, and A. Smolyanitsky, *The Journal of Physical Chemistry C* **123**, 3588 (2019).  
 [6] S. Sahu, J. Elenewski, C. Rohmann, and M. Zwolak, *Science Advances* **5**, eaaw5478 (2019).  
 [7] A. Smolyanitsky, A. Fang, A. F. Kazakov, and E. Paulechka, *Nanoscale* **12**, 10328 (2020).  
 [8] S. Sahu and M. Zwolak, *Entropy* **22**, 1326 (2020).  
 [9] L. Jubin, A. Poggioli, A. Siria, and L. Bocquet, *Proceedings of the National Academy of Sciences* **115**, 4063 (2018).  
 [10] T. Mouterde, A. Keerthi, A. Poggioli, S. A. Dar, A. Siria, A. K. Geim, L. Bocquet, and B. Radha, *Nature* **567**, 87 (2019).  
 [11] X. Jiang, C. Zhao, Y. Noh, Y. Xu, Y. Chen, F. Chen, L. Ma, W. Ren, N. R. Aluru, and J. Feng, *Science Advances* **8**, eabj2510 (2022).  
 [12] C. E. Morris and W. J. Sigurdson, *Science* **243**, 807 (1989).  
 [13] A. Franco Jr and J. B. Lansman, *Nature* **344**, 670 (1990).  
 [14] A. Franco, B. D. Winegar, and J. B. Lansman, *Biophysical journal* **59**, 1164 (1991).  
 [15] A. Franco-Obregón and J. B. Lansman, *The Journal of physiology* **539**, 391 (2002).  
 [16] S. Sukharev, M. Betanzos, C.-S. Chiang, and H. R. Guy, *Nature* **409**, 720 (2001).  
 [17] N. Alem, R. Erni, C. Kisielowski, M. D. Rossell, W. Gannett, and A. Zettl, *Physical review B* **80**, 155425 (2009).  
 [18] J. Zhang, R. Sun, D. Ruan, M. Zhang, Y. Li, K. Zhang, F. Cheng, Z. Wang, and Z.-M. Wang, *Journal of Applied Physics* **128** (2020).  
 [19] J. Mahmood, E. K. Lee, M. Jung, D. Shin, I.-Y. Jeon, S.-M. Jung, H.-J. Choi, J.-M. Seo, S.-Y. Bae, S.-D. Sohn, et al., *Nature Communications* **6**, 6486 (2015), ISSN 2041-1723.  
 [20] Y. Yang, W. Li, H. Zhou, X. Zhang, and M. Zhao, *Scientific Reports* **6**, 29218 (2016), ISSN 2045-2322.  
 [21] M. L. Barabash, W. A. T. Gibby, C. Guardiani, D. G. Luchinsky, B. Luan, A. Smolyanitsky, and P. V. E. McClintock, *The Journal of Physical Chemistry B* **125**, 7044 (2021), ISSN 1520-6106.  
 [22] W. L. Jorgensen, J. Chandrasekhar, J. D. Madura, R. W. Impey, and M. L. Klein, *The Journal of chemical physics* **79**, 926 (1983).  
 [23] W. L. Jorgensen, D. S. Maxwell, and J. Tirado-Rives, *Journal of the American Chemical Society* **118**, 11225 (1996).  
 [24] A. Govind Rajan, M. S. Strano, and D. Blankschtein, *The journal of physical chemistry letters* **9**, 1584 (2018).  
 [25] C. M. Breneman and K. B. Wiberg, *Journal of Computational Chemistry* **11**, 361 (1990).  
 [26] C. Lee, W. Yang, and R. G. Parr, *Phys. Rev. B* **37**, 785 (1988).  
 [27] A. D. Becke, *The Journal of Chemical Physics* **98**, 5648

- (1993), ISSN 0021-9606.
- [28] M. J. Abraham, T. Murtola, R. Schulz, S. Páll, J. C. Smith, B. Hess, and E. Lindahl, *SoftwareX* **1**, 19 (2015).
- [29] S. Páll, A. Zhmurov, P. Bauer, M. Abraham, M. Lundborg, A. Gray, B. Hess, and E. Lindahl, *The Journal of Chemical Physics* **153** (2020).
- [30] See Supplemental Material at [URL will be inserted by publisher] for additional data, parametric studies, as well as discussions of interaction scaling and transport types.
- [31] J. P. Perdew, K. Burke, and M. Ernzerhof, *Phys. Rev. Lett.* **77**, 3865 (1996).
- [32] C. Hartwigsen, S. Goedecker, and J. Hutter, *Phys. Rev. B* **58**, 3641 (1998).
- [33] J. VandeVondele and J. Hutter, *J. Comp. Phys.* **127**, 114105 (2007).
- [34] S. Grimme, J. Antony, S. Ehrlich, and H. Krieg, *The Journal of Chemical Physics* **132**, 154104 (2010), ISSN 0021-9606.
- [35] G. Hummer, L. R. Pratt, and A. E. Garcia, *J. Phys. Chem.* **100**, 1206 (1996).
- [36] J. S. Hub, B. L. De Groot, and D. van der Spoel, *Journal of chemical theory and computation* **6**, 3713 (2010).